International Journal of Refractory Metals and Hard Materials 116 (2023) 106364

Contents lists available at ScienceDirect

International Journal of Refractory Metals and Hard Materials

journal homepage: www.elsevier.com/locate/IJRMHM

Damage characterisation of tantalum ion source electrodes and reconditioning by wire- and powder-based laser metal deposition

Tobia Romano [a,b,*], Dagnija Kroģere [b], Andris Ratkus [b,c], Hannes Lauer [d], Franz Marquardt [d], Maurizio Vedani [a], Diego Obradors [e], Markus Weinmann [f], Toms Torims [b,c]

[a] Department of Mechanical Engineering, Politecnico di Milano, Milan, Italy
[b] Centre of High-Energy Physics and Accelerator Technologies, Riga Technical University, Riga, Latvia
[c] The European Organization for Nuclear Research (CERN), Meyrin, Switzerland
[d] Fraunhofer Institute for Material and Beam Technology (IWS), Dresden, Dresden, Germany
[e] Department of Technology, Centro de Investigaciones Energéticas, Medioambientales y Tecnológicas (CIEMAT), Madrid, Spain
[f] Taniobis GmbH, Goslar, Germany

ARTICLE INFO

Keywords:
Laser metal deposition
Tantalum
Additive manufacturing
Repair
PIG ion source
Abnormal grain growth

ABSTRACT

The internal ion source of the Advanced Molecular Image Technologies (AMIT) superconducting cyclotron uses cathodes made of pure tantalum to generate high energy H^- ion beams for the production of isotopes for positron emission tomography. During service, the cathodes are impacted by high-energy ions from the plasma. The resulting erosion creates craters that reduce the current density of the extracted beam. The cathodes eventually need to be replaced when the ion source can no longer be activated. This research explores the possibility of repairing the tantalum cathodes used in the AMIT cyclotron through laser metal deposition additive manufacturing. The damaged parts were first characterised by 3D imaging, scanning electron microscopy, and Vickers microhardness to understand the damage mechanisms occurring during service and quantify the extent of the damage. Different repair strategies were then tested employing both high-purity tantalum wire and powder feedstocks and the properties of the reconditioned electrodes were determined. The ability of laser metal deposition to restore the damaged cathodes for use in the AMIT cyclotron has been demonstrated.

1. Introduction

Due to its excellent high-temperature stability, corrosion resistance, and biocompatibility, tantalum is employed in specialised applications in the electronics, aerospace, nuclear, chemical, biomedical, and military fields [1,2]. Tantalum is also used to manufacture components for particle accelerators [3], such as the cathodes used in the Penning Ionisation Gauge (PIG) ion source of the compact superconducting cyclotron developed within the Advanced Molecular Image Technologies (AMIT) project [4,5] (Fig. 1a). The PIG ion source used by the AMIT cyclotron installed at Centro de Investigaciones Energéticas, Medioambientales y Tecnológicas (CIEMAT) in Madrid consists of a hollow anode made of a copper-tungsten alloy and two electrodes (a cathode and an anticathode) made of 99.95% pure tantalum. The ion source operates in a pure hydrogen atmosphere to generate high-energy H^- ion beams for the production of ^{18}F and ^{11}C isotopes for positron emission tomography (PET) [4,6]. Tantalum is employed owing to its high melting point (3017 °C), low discharge voltage (1700 V), low work function (4.25 eV), and low sputtering coefficient in H_2 (16 mg/Ah) [3,7,8].

During operation, the voltage applied between the electrodes causes emission of electrons from the cathode. Emitted electrons are accelerated towards the opposite cathode by the potential difference, following a helical orbit across the hollow anode due to an applied axial magnetic field (Fig. 1b). Positive and negative hydrogen ions (H^+ and H^- ions, respectively) are produced by collision of electrons with the gas molecules in the working chamber. As a result, a plasma is formed. H^- ions are extracted through a slit opening on the hollow anode by a puller biased with an alternating potential, during the positive half periods of the potential. On the other hand, H^+ ions are accelerated towards the anticathode and impinge on it with a typical energy of several hundred eV. These collisions locally increase the temperature of the cathode and promote the emission of secondary electrons by thermionic effect. Although this is essential to sustain the glow discharge and produce the

* Corresponding author at: Department of Mechanical Engineering, Politecnico di Milano, 34 La Masa, Milan 20156, Italy.
E-mail address: tobia.romano@polimi.it (T. Romano).

https://doi.org/10.1016/j.ijrmhm.2023.106364
Received 17 May 2023; Accepted 10 August 2023
Available online 17 August 2023

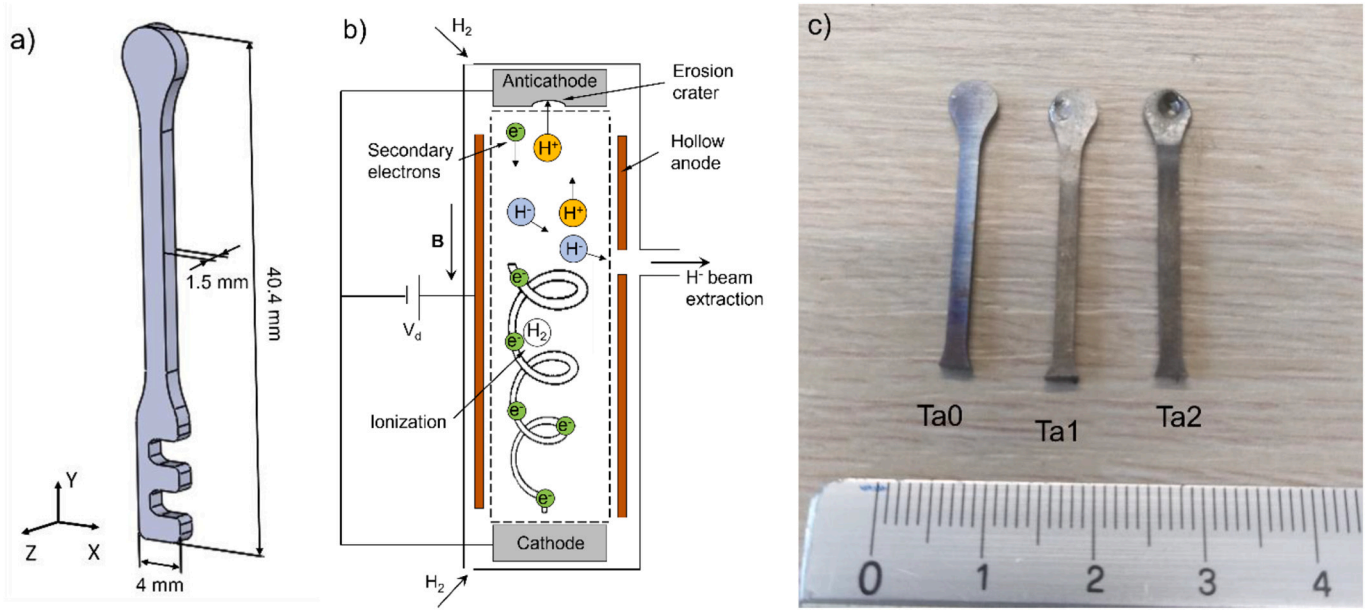

Fig. 1. Schematics of tantalum cathodes (a) and AMIT cyclotron ion source design (b), and photograph of the unused (Ta0) and worn (Ta1 and Ta2) cathodes (c). Adapted from [6].

ion beam, after a variable running time a crater-shaped erosion profile appears on the surface of the electrodes in the region that is subjected to ion bombardment (Fig. 1c). This delays thermionic emission and reduces the current density of the extracted beam [5]. When a relatively large amount of material is removed, the ion source can no longer be operated. The current practice is to simply replace the worn cathodes with new parts, since the damage mechanisms to which they are subjected and how they affect their performance are not yet fully understood.

The need to periodically replace the cathodes increases the operating costs of the AMIT cyclotron [5]. In addition, tantalum is considered a critical raw material because it is widely employed in various industrial fields, but its supply chain has often been subjected to fluctuations and

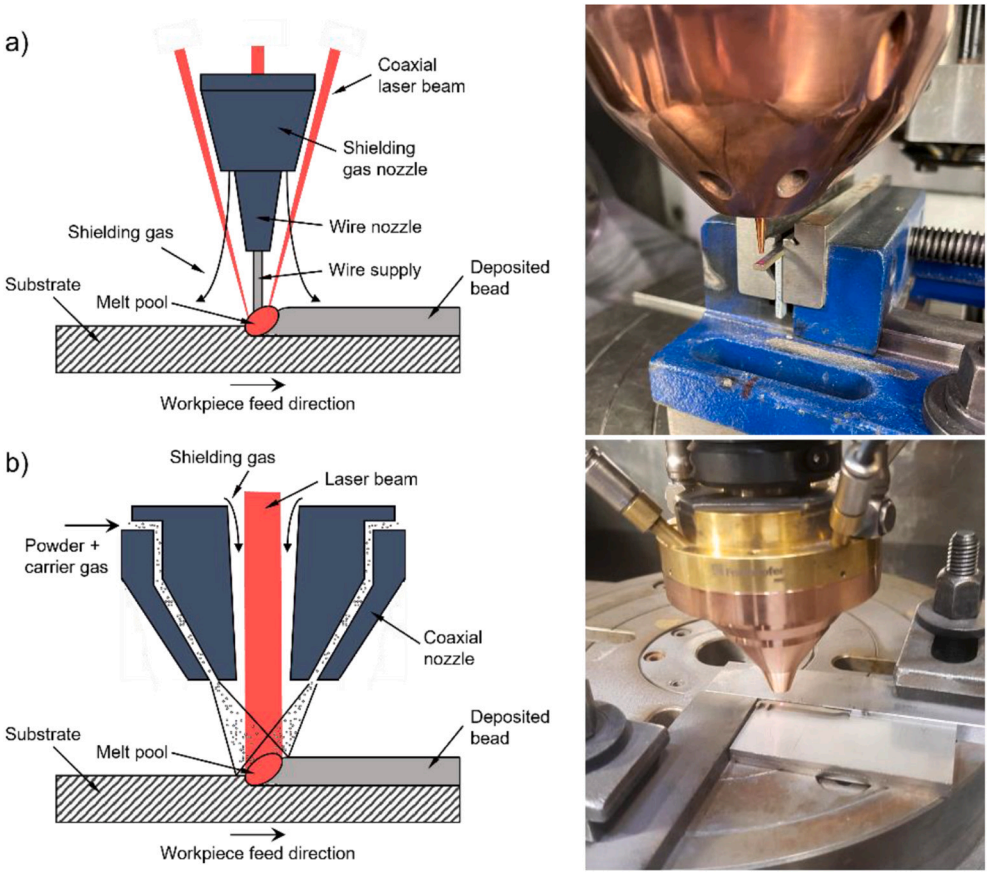

Fig. 2. Schematic and photograph of the LMD experimental setup using wire (a) and powder (b) feedstocks. Adapted from [23,24].

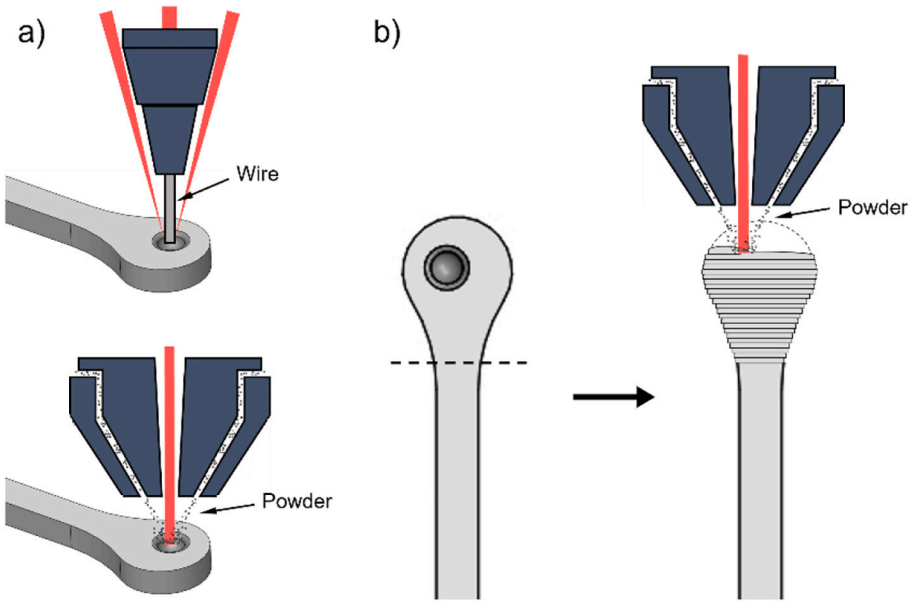

Fig. 3. Schematic of repair strategies based on erosion crater filling (a) and full head rebuild (b).

disruption [9]. Therefore, it would be not only economically advantageous, but likewise sustainable, to restore the worn electrodes after they have become inoperable, instead of replacing them with new parts.

In recent years, the ability of additive manufacturing (AM) technologies to repair and restore various kinds of industrial components has been demonstrated [10–12]. Among these, laser metal deposition (LMD) is particularly suited for repair, as it uses a robotic arm equipped with a laser source and a dispenser to add material to existing parts. Its high flexibility combined with the use of a highly focused laser beam enables the repair of damaged structures with good dimensional accuracy, minimal distortion, and excellent metallurgical bonding between the substrate and the added material [13]. AM of pure tantalum has been mainly investigated in the context of laser powder bed fusion (LPBF) and electron beam powder bed fusion (EB-PBF) for the manufacturing of orthopaedic implants [14–18], and wire arc additive manufacturing (WAAM) to produce larger components for the aerospace and chemical industries [7,19]. LMD has also been applied to fabricate pure tantalum parts [20] and deposit tantalum coatings to improve the osseointegration of titanium implants [21]. However, to the best of authors' knowledge, no attempts to repair tantalum components have been reported in the literature so far.

In the present study, wire- and powder-based LMD technologies are proposed for repairing the worn tantalum cathodes used in the AMIT superconducting cyclotron. Damaged parts were first characterised to understand the damage mechanisms occurring during service and to quantify the extent of the damage in order to devise appropriate restoration strategies. After optimisation of the process parameters, representative pure tantalum cathodes with different degrees of damage were reconditioned and then characterised to compare their properties with those of the original parts.

2. Materials and methods

2.1. Electrode characterisation

Initial characterisation analyses were performed on a reference unused tantalum electrode (Ta0) for comparison purposes, on a slightly worn electrode having a shallow crater (Ta1), and on a heavily worn electrode with a deeper crater (Ta2), as shown in Fig. 1b.

The shape of the crater of each worn cathode was determined by optical 3D measurements, employing an Alicona InfiniteFocus instrument. The parts were previously covered by a thin graphite layer to avoid excessive light reflection during the measurement. The surface morphology and microstructure of the electrodes were studied using a Nikon Eclipse LV150NL optical microscope and a Zeiss Sigma 500 field-emission scanning electron microscope (FE-SEM) equipped with an Oxford Instruments energy dispersive X-ray spectrometer (EDS) and an electron back-scattered diffraction (EBSD) detector. For microstructural observation, the specimens were first sectioned by a precision diamond-blade saw, mounted in thermosetting resin, grinded with SiC papers up to 2500 grit, and finally polished with 10% water-based 0.5 μm alumina and 0.03 μm silica suspensions. An additional vibratory polishing step was conducted for EBSD analyses using a 25% water-based 0.03 μm silica colloidal suspension. Chemical etching was performed using a fresh solution prepared with 10 ml H_2SO_4, 5 ml HF, and 5 ml HNO_3.

Vickers microhardness measurements were performed on the polished samples with a Future-Tech FM-700 microhardness tester. A load of 500 g was applied for a dwell time of 10 s in each test repetition.

2.2. Development of LMD repair strategies

LMD repair tests were conducted using wire and powder feedstocks, respectively. The wire-based process was carried out using the COAX-wire mini laser deposition head developed at Fraunhofer Institute for Material and Beam Technology IWS (Dresden) (Fig. 2a) [22]. The LMD machine was equipped with a 1 kW TRUMPF TruDisk 1000 laser having 1064 nm wavelength and fed with a 99.95% pure tantalum wire 0.5 mm in diameter. In the powder-based process, a COAX14 annular gap nozzle and a Laserline LDF laser with 1080 nm wavelength and 1.1 mm spot size were used for material deposition (Fig. 2b). The AMtrinsic® 99.9% pure tantalum powder provided by Taniobis, having spherical morphology and 10–63 μm particle size, was used as feedstock material. In both cases, argon shielding gas was continuously delivered to the melt region.

Two different repair strategies were tested in preliminary LMD trials. The first approach was to deposit the material inside the erosion craters to restore the original electrode morphology (Fig. 3a). Due to the limited availability of representative tantalum test pieces, it was not possible to conduct a robust study for the optimisation of all the process parameters. However, the effects of wire feed rate, oxygen content in the local shielding atmosphere, and substrate preheating condition were evaluated in the wire-based process in order to obtain high-quality deposits.

Table 1
Process parameters used in multilayer powder-based LMD tests.

Parameter	Value
Laser power (W)	1200
Powder feed rate (g s^{-1})	2.55
Carrier gas flow rate (l min^{-1})	6
Deposition speed (mm min^{-1})	300
Layer thickness (mm)	0.3
Cooling time between layers (s)	30

The microstructure of specimens manufactured under the different experimental conditions was characterised using an Olympus GX51 optical microscope. Metallographic preparation involved grinding with 220, 500, and 1200 grit abrasive papers and polishing using a compound prepared with 200 ml CH_3OH, 40 ml H_2O_2, 1 ml HNO_3, and few drops of HF. The etching solution was prepared with water, HCl, HNO_3, and HF in equal parts. The second strategy was to cut off the damaged head of the electrodes and build a new one starting from the top end of the remaining stem (Fig. 3b). Multilayer build-up tests were conducted through powder-based LMD using the parameters that resulted in single track deposits free of interface and lack of fusion porosity (Table 1).

2.3. LMD repair and characterisation of reconditioned electrodes

The strategy adopted to refurbish representative damaged electrodes consisted of depositing material inside the erosion craters to restore the original electrode morphology. Three tantalum cathodes with varying extent of damage were reconditioned with each LMD technique (Fig. 4).

Regarding the wire-based process, the erosion craters were simply filled with a single dot of material, as shown in Videos 1–3. Since the volume of deposited material depends on the duration of the process, a short deposition time of 0.2 s was used to refurbish the electrode with the smallest crater (W1). The deposition time was conveniently increased for the electrodes with medium and large crater size (W2 and W3, respectively). The main process parameters for the wire-based repair are listed in Table 2.

The scanning strategy selected for the powder-based process involved the deposition of three concentric rings inside the erosion crater, starting from the inner circle. The radius of the external circle was set depending on the extension of the damaged zone (larger for electrode P1). On the other hand, the deep crater of electrode P3 was partially filled by depositing two dots of material before building the concentric rings. Table 3 reports the main process parameters used in the powder-based repair operations.

After repair, the electrodes W2 and P2 were cut, mounted in resin, and polished for SEM, EBSD, and microhardness analyses following the same procedures described above. A part used in one of the powder-based LMD preliminary trials was grinded using a 320-grit SiC abrasive paper to demonstrate that a surface finishing similar to that of the original electrodes can be achieved through a simple post-processing operation.

Table 2
Process parameters for wire-based LMD repair.

Parameter	Electrode		
	W1	W2	W3
Laser power (W)	1000	1000	1000
Wire feed rate (mm s^{-1})	50 (start/end speed) 20 (normal speed)	50 (start/end speed) 20 (normal speed)	50 (start/end speed) 20 (normal speed)
Shielding gas pressure (bar)	2.5	2.5	2.5
Oxygen content (ppm)	300	300	300
Preheating time (s)	1	1	1
Deposition time (s)	0.2	0.4	0.6

Table 3
Process parameters for powder-based LMD.

Parameter	Electrode		
	P1	P2	P3
Laser power (W)	800	800	800
Powder feed rate (g s^{-1})	2	2	2
Carrier gas flow rate (l min^{-1})	6	6	6
Shielding gas flow rate (l min^{-1})	12	12	12
Deposition speed (mm min^{-1})	400 (inner circle) 600 (middle circle) 600 (external circle)	400 (inner circle) 600 (middle circle) 600 (external circle)	400 (inner circle) 600 (middle circle) 600 (external circle)
Circle radius (mm)	0.4 (inner circle) 0.9 (middle circle) 1.5 (external circle)	0.4 (inner circle) 0.9 (middle circle) 1.2 (external circle)	0.4 (inner circle) 0.9 (middle circle) 1.2 (external circle)
Deposition time for dots (s)	–	–	0.5

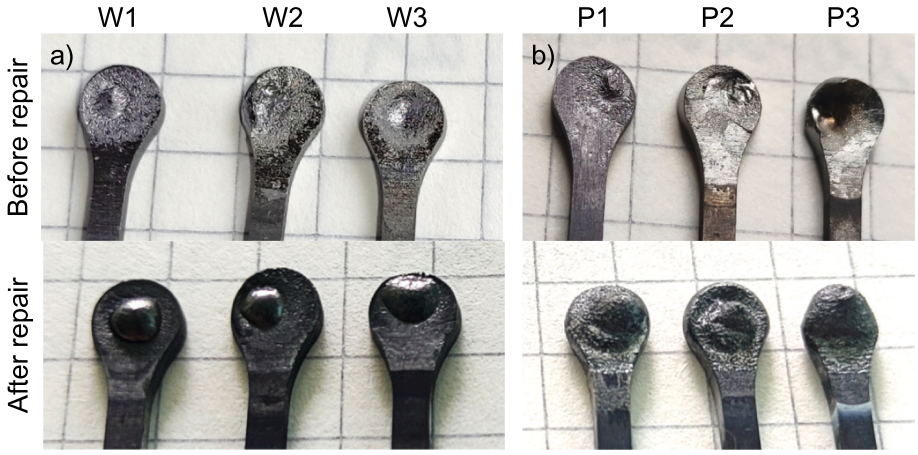

Fig. 4. View of electrodes repaired with wire- (a) and powder-based LMD (b).

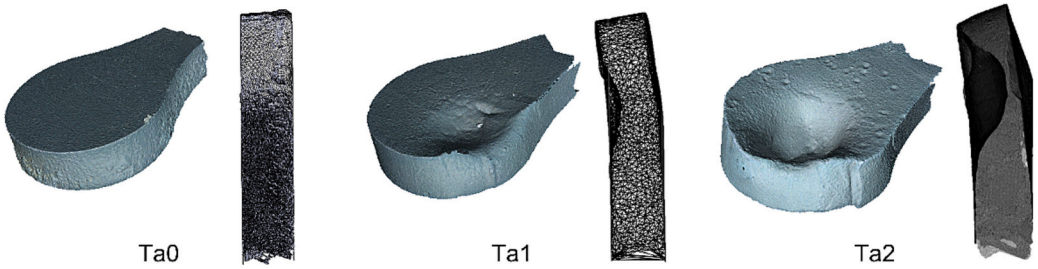

Fig. 5. 3D images of the unused and worn tantalum electrodes.

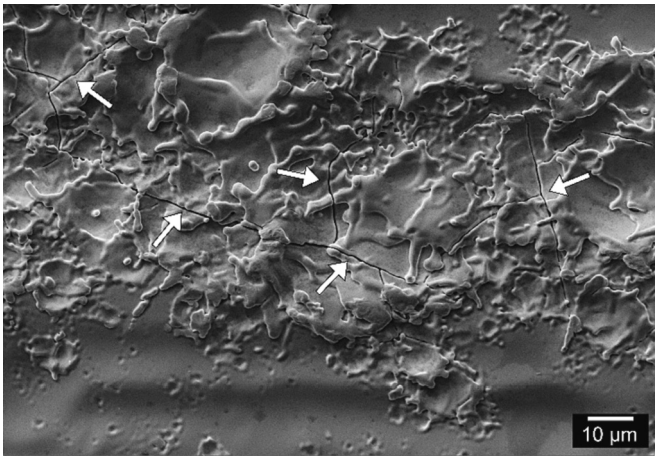

Fig. 6. Evidence of local melting on electrode Ta1.

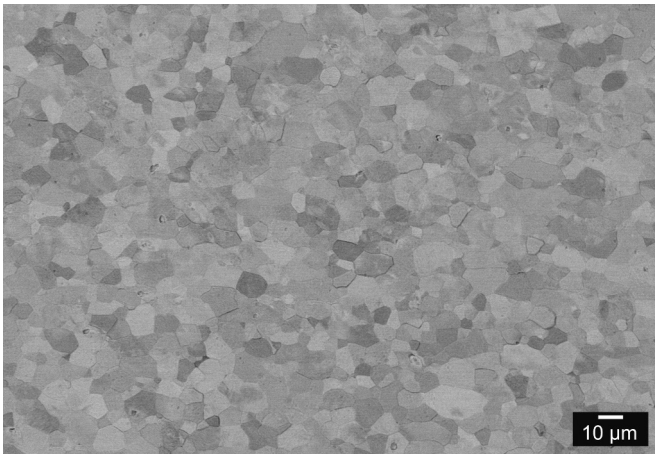

Fig. 7. Fine equiaxed microstructure of the unused electrode Ta0.

3. Results and discussion

3.1. Characterisation of unused and damaged electrodes

Figure 5 shows the 3D reconstruction of the head region of the cathode samples. A shallow erosion crater displaced from the head centre is observed on both worn electrodes Ta1 and Ta2. This indicates that ion sputtering was concentrated on a limited area during operation in the cyclotron. The regions around the crater appear severely pitted from the impact of ions. In addition, the presence of droplets of re-solidified material (Fig. 6) indicates that the material reached extremely high local temperatures under the action of the high-energy ions impinging on the electrode surface. The cracks highlighted with arrows in Fig. 6 may have been caused either by shrinkage stress upon re-solidification of the small molten volume or by volume expansion produced by hydrogen absorption [25], since the cathode was kept in a pure hydrogen atmosphere during operation in the cyclotron.

While the initial material exhibits a homogeneous equiaxed microstructure with average grain size of about 8.5 µm (Fig. 7), the head of the worn electrodes comprises of few extremely coarse grains, as highlighted in the EBSD images of Fig. 8. Pedrazas et al. [26] demonstrated that pure tantalum undergoes dynamic abnormal grain growth (DAGG) when plastically deformed at temperature higher than 1450 °C. The fast grain boundary migration leads to the formation of abnormally coarse grains, with size up to several tens of millimetres. Abnormal grain growth may have been promoted by the high temperature and the plastic deformation experienced by the electrodes due to the impact of high-energy ions. The macroscopic deformation of the head of the cathode Ta2 was accompanied by the formation of a large twin visible in the inverse pole figure (IPF) map of Fig. 8b, as identified by the measured 60° misorientation angle about ⟨111⟩ direction (inset of Fig. 8b), which is typical of body-centred cubic crystals [27].

A progressive increase in the grain size was observed along the stem length of the electrodes Ta1 and Ta2, from about 8.5 µm at the base, to more than 100 µm in the regions just below the head (Fig. 9a-f), up to the abnormally coarse grains at the cathode head (Fig. 8). This variation is attributed to the higher temperature experienced by the material near the head of each electrode, where ion bombardment concentrated during operation in the cyclotron.

Although a larger grain size is normally associated with a lower hardness, the Vickers microhardness progressively increases from about 100 $HV_{0.5}$, corresponding to the hardness of the original material, to over 700 $HV_{0.5}$, as shown in Fig. 9g. Since no hard second phases nor a significant increase in the content of strengthening interstitial elements [20,28] were detected, this trend may be attributed to hydrogen- and ion-irradiation-induced hardening. Previous results showed that hydrogen can have a hardening effect in other metals featuring a body-centred cubic crystal structure, like pure iron [29] and ferritic-pearlitic steel [30], when its content is high and hydrogen atoms are trapped by strong trapping sites. Under these conditions, hydrogen atoms tend to segregate to form atmospheres around dislocations, producing a pinning and dragging effect that hinders the motion of dislocations, thus increasing the hardness of the material [29–31]. Although this effect is more likely to occur when large amounts of hydrogen are introduced by electrochemical charging than by simple exposure to a hydrogen gas environment [30], Takagi et al. [32] demonstrated that vacancy clusters acting as strong trapping sites for deuterium atoms can be introduced in tantalum by bombarding it with high-energy ions. Therefore, ion bombardment during cyclotron operation may have introduced hydrogen traps in the tantalum electrodes, promoting hydrogen entrapment and resulting in the increasing hardness measured along the body of the serviced cathodes. In addition, sessile dislocation loops produced in pure tantalum by H^+ ion (i.e., proton) irradiation [33] can interact with edge dislocations, reducing their mobility and leading to an increase in hardness [34].

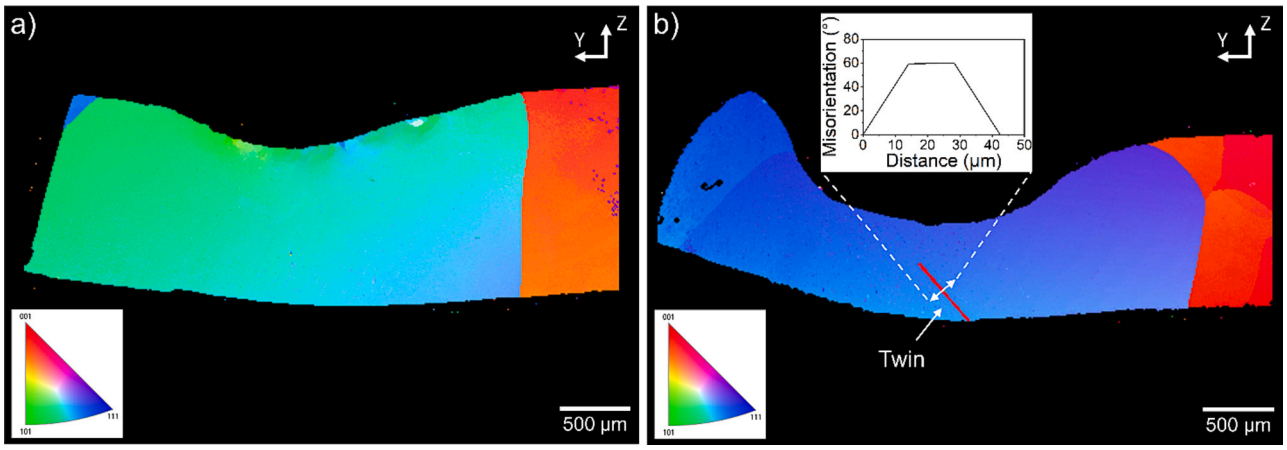

Fig. 8. Abnormally coarse grain structure at the head of electrodes Ta1 (a) and Ta2 (b).

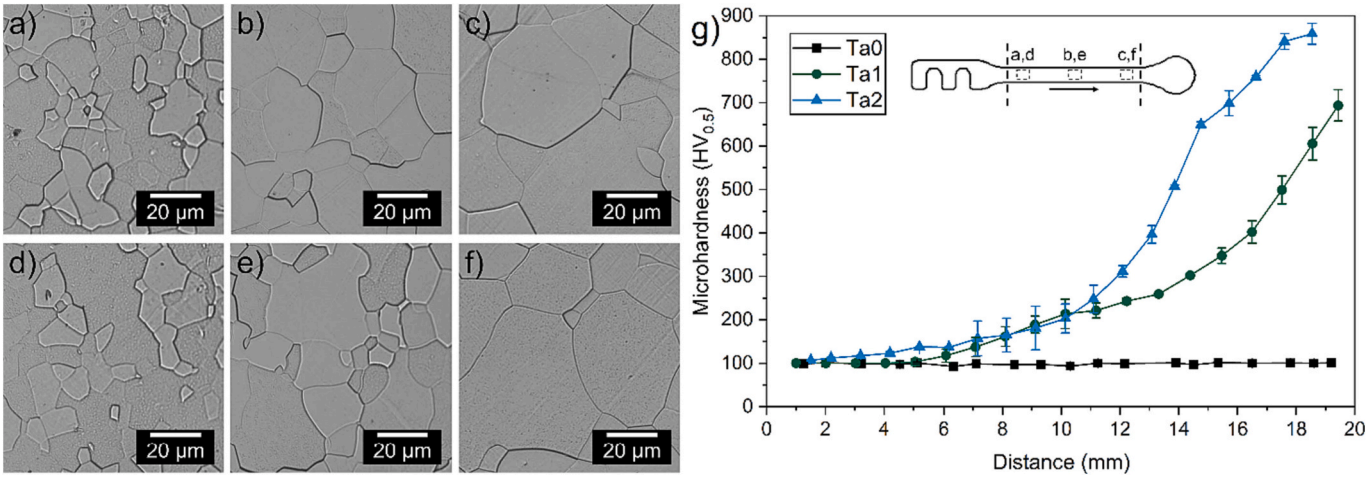

Fig. 9. Grain size variation along the body of electrodes Ta1 (a-c) and Ta2 (d-f) and corresponding microhardness profile (g).

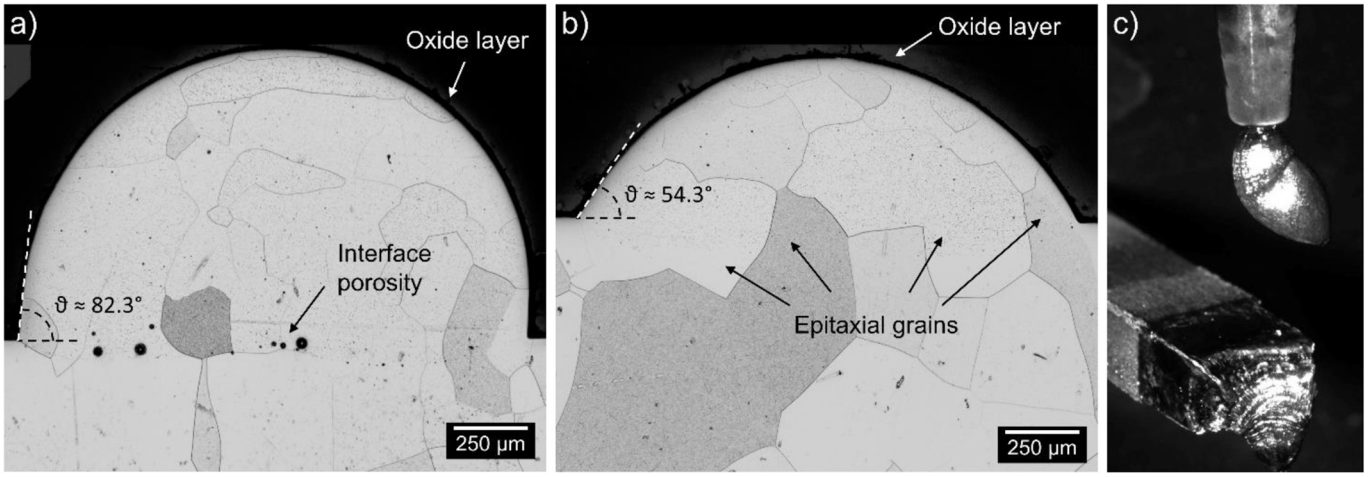

Fig. 10. Microstructure of deposits produced by wire-based LMD without (a) and with laser substrate preheating (b), and effect of insufficient start wire feed rate (c).

3.2. Development of LMD parameters

Although an in-depth optimisation study was not conducted due to the few available tantalum test samples, the effects of experimental conditions on the quality of LMD deposits were investigated by varying the main process parameters. As regards the wire-based process, it was observed that the substrate material needs to be preheated prior to the deposition process to avoid excessive residual porosity at the interface and improve dilution with the substrate. A 1000 W laser preheating of 1 s effectively eliminated the interface porosity, reduced the clad angle (ϑ), and improved the metallurgical bonding between the LMD deposit and the substrate, as shown in Fig. 10a-b. The grain structure of the

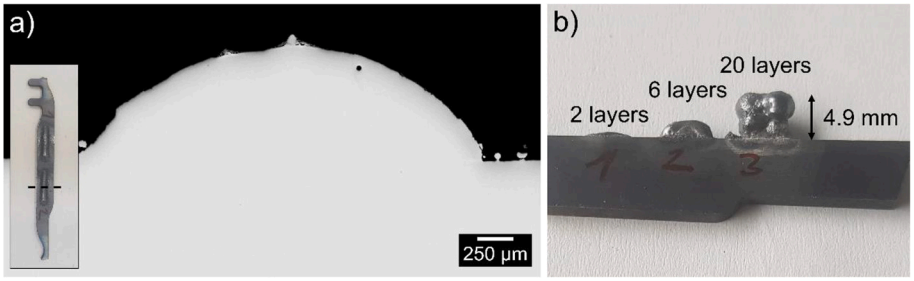

Fig. 11. Near defect-free single track (a) and multilayer structures deposited by powder-based LMD (b).

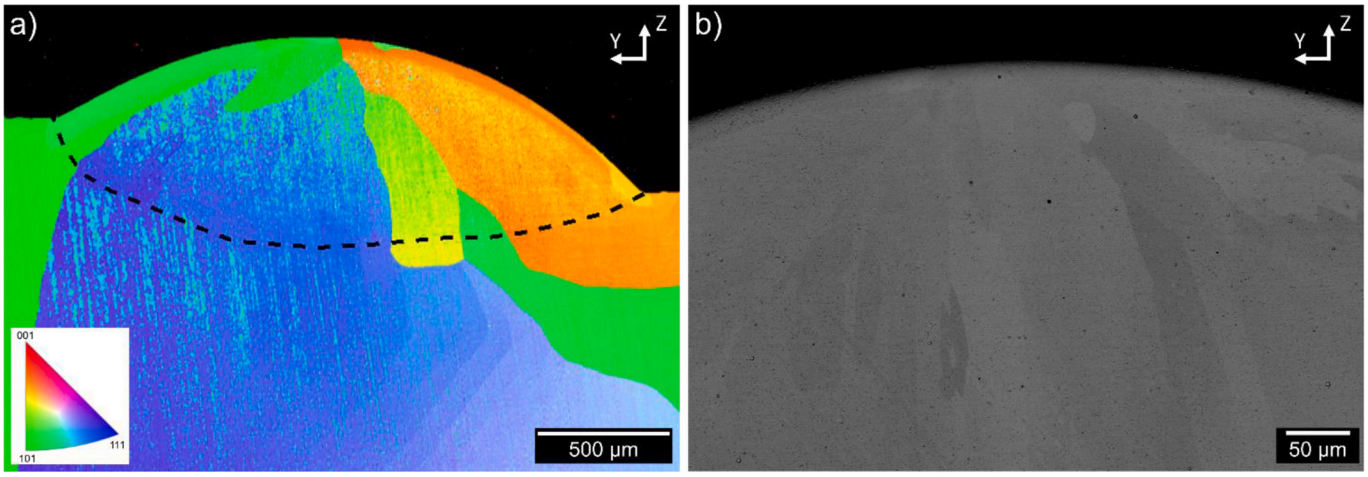

Fig. 12. EBSD (a) and SEM (b) images of the electrode W2 repaired by wire-based LMD.

dome deposited with laser preheating (Fig. 10b) featured almost equiaxed grains, which initially grew epitaxially from the grains of the substrate. However, it was noted that the substrate should not be exposed to a laser power of 1000 W for more than 1.5 s to avoid melting. An oxygen content of ~12% in the local shielding atmosphere led to the formation of a distinct oxide layer on the surface of the deposits, as highlighted in Fig. 10a-b. Therefore, the oxygen content was reduced to 300 ppm in the actual repair operations by generating a shielding gas bell around the melt pool region. Regarding the deposition strategy, it was observed that the wire must be fed at a higher rate at the beginning and end of the process to prevent it from melting before it has reached the substrate, generating a ball of melted and resolidified material that cannot be deposited correctly (Fig. 10c and Video 4).

Laser power, powder feed rate, and scanning speed were adjusted in the powder-based process by depositing several clad beads and domes consisting of concentric circles. The combination of parameters leading to deposits with no lack of fusion porosity at the interface with the substrate (Fig. 11a) was employed in multilayer build-up tests, as indicated in Table 1. Based on previous experience, a cooling time of 30 s was applied between the deposition of two successive layers to avoid overheating and keep the interlayer temperature below 250 °C. Despite this, after depositing the first ten layers, the material underwent creep flow and the target geometry could not be attained (Fig. 11b). Guan et al. [20] successfully manufactured pure tantalum thin-walled plates

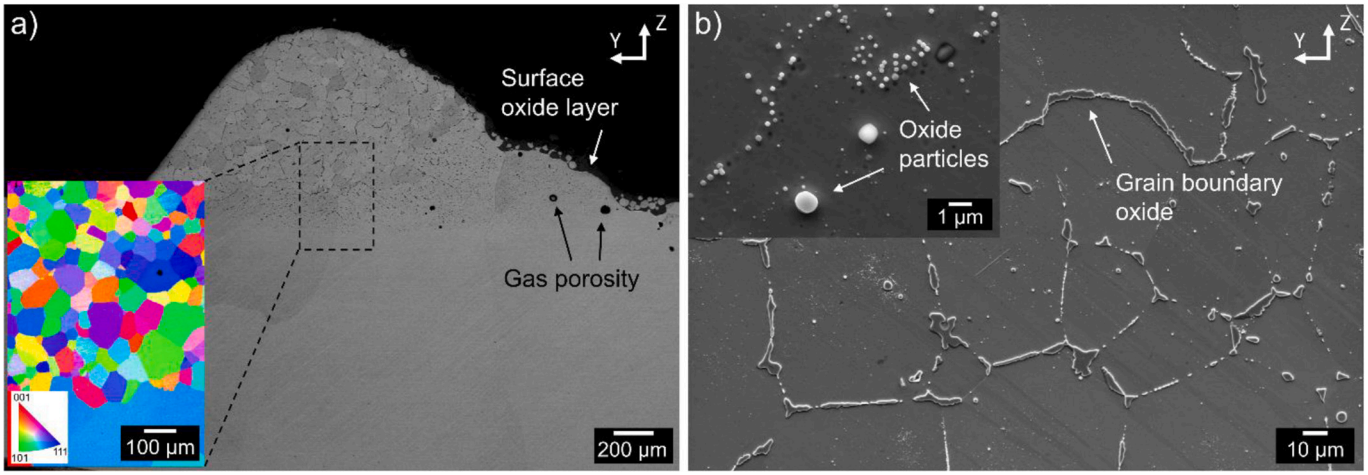

Fig. 13. SEM images of the electrode P2 repaired by powder-based LMD.

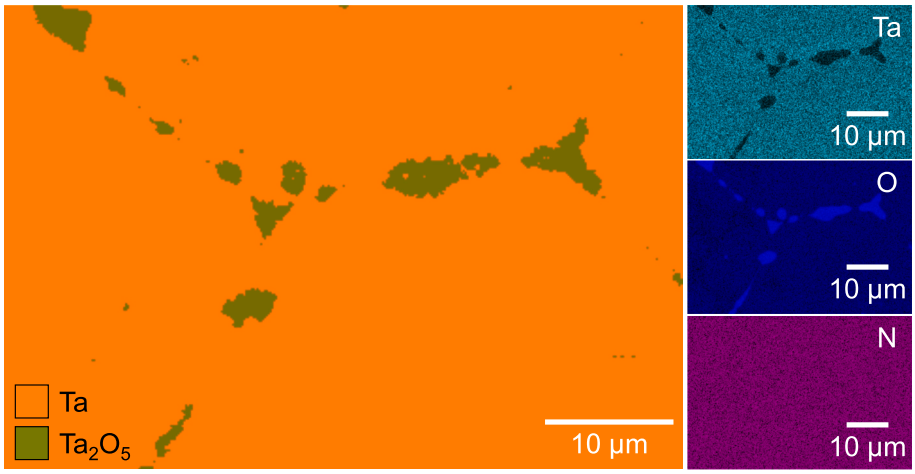

Fig. 14. Phase and elemental maps of powder-based LMD deposit.

by depositing several layers using powder-based LMD. However, the small size of the multilayer deposits tested in the present study probably resulted in a poorer dissipation of the input heat during the deposition process, giving rise to the observed flowing phenomenon. Therefore, further research efforts need to be dedicated to better adjust the process parameters to pursue the repair strategy based on printing a new electrode head to replace the damaged one.

3.3. Characterisation of repaired electrodes

The EBSD image of Fig. 12a shows the cross-section of the electrode W2 repaired with the wire-based process by depositing one dot of material inside the crater. The LMD deposit, highlighted by the dotted line, is composed of few large grains grown epitaxially from the substrate, as they have the same crystallographic orientations as the grains beneath. Additively manufactured tantalum typically exhibits coarse columnar grains with a ⟨111⟩ preferential orientation aligned along the build direction [19,35]. This microstructure develops in pure tantalum because favourably oriented ⟨111⟩ grains [36,37] tend to grow along the direction of maximum heat flow towards the substrate [38], that acts as a heat sink. In the present case, large columnar grains could not develop because only one dot of material was deposited. Therefore, edge effects dominated the solidification [35]. Only few dispersed pores smaller than 10 μm in size can be seen in the micrographs. In addition, there are no distinct signs of oxide layers (Fig. 12b), indicating that the employed shielding gas bell effectively protected the material against oxidation at high temperature during the repair process. An oxygen content of about 0.8 wt% was detected by EDS analysis. Although this technique cannot provide a very precise measure of the content of light elements, this value is comparable to that measured for the unused electrode (~0.5 wt %). More accurate measurements could not be performed due to the small size of the specimen.

Figure 13a shows the cross-section of the electrode P2 repaired with the powder-based process. The LMD deposit is composed of randomly oriented equiaxed grains with average size around 52 μm, as shown in the EBSD image in the inset of Fig. 13a. Unlike the wire-based process, the substrate could not be preheated in powder-based LMD because the laser could only be turned on after the powder flow had already been established. Hence, the deposited material in contact with the cold substrate experienced a higher cooling rate, generating the finer grains observed. Balla et al. [21] found a similar microstructure in tantalum coatings of comparable thickness applied to titanium substrates by laser deposition, but with a slightly larger grain size (about 70 μm). The lower average grain size observed here can be attributed to the higher thermal conductivity of the tantalum substrate compared to titanium, resulting in a faster cooling. The large columnar grains that develop in pure tantalum parts fabricated by multilayer LMD [20] were not observed because no significant competitive growth occurred by depositing concentric rings in the same plane.

Table 4
Vickers microhardness of deposits made by wire- and powder-based LMD in comparison with the original material.

	Electrode		
	Ta0	W2	P2
Microhardness ($HV_{0.5}$)	98.9 ± 2.4	315.3 ± 10.3	665.4 ± 19.0

Observation of high magnification SEM images revealed that fine precipitates decorate the grain boundaries and extremely fine particles (less than 300 nm in diameter) are also dispersed within the grains, as depicted in Fig. 13b. The phase and elemental maps collected from the EBSD and EDS analyses (Fig. 14) indicate that these scales are Ta_2O_5 particles, possibly formed due to turbulence in the shielding gas flow during the LMD process caused by the carrier gas conveying the powder particles towards the melt pool [39]. The overall oxygen content measured by EDS is around 3 wt%. In addition, a distinct oxide layer about 60 μm in thickness continuously covers the external surface of the deposited dome, as highlighted in Fig. 13a. This must have formed at the end of the deposition process, when the already solidified but still hot metal was exposed to environmental oxygen once the shielding gas flow was turned off. This oxide layer may have a beneficial effect by increasing the secondary emission coefficient of the material (i.e., the ratio of the emitted secondary electrons to the incident primary electrons), thus helping to sustain the glow discharge and produce the ion beam [3,40]. However, its actual effect on the electrode performance still needs to be evaluated by testing the restored cathodes under service conditions. The round pores located at the interface between the substrate and the deposited dome (Fig. 13a) may have been generated by gases trapped inside the molten bath during the deposition process [38].

Table 4 compares the Vickers microhardness of the repaired electrodes with that of the original material. The microhardness of the deposit made with the wire-based process is similar to that reported for tantalum parts and coatings fabricated by direct laser deposition [20,21] and slightly lower than pure tantalum processed through LPBF [14]. This can be attributed to the slower cooling rates of LMD compared to LPBF [38], typically resulting in a coarser microstructure, and to the very small size of the electrodes, leading to poor dissipation of the process input heat. The high hardness of the deposit made using the powder feedstock can be primarily attributed to the fine oxide particles observed both at the grain boundaries and dispersed within the grains, providing a precipitation hardening effect. Another contribution is due

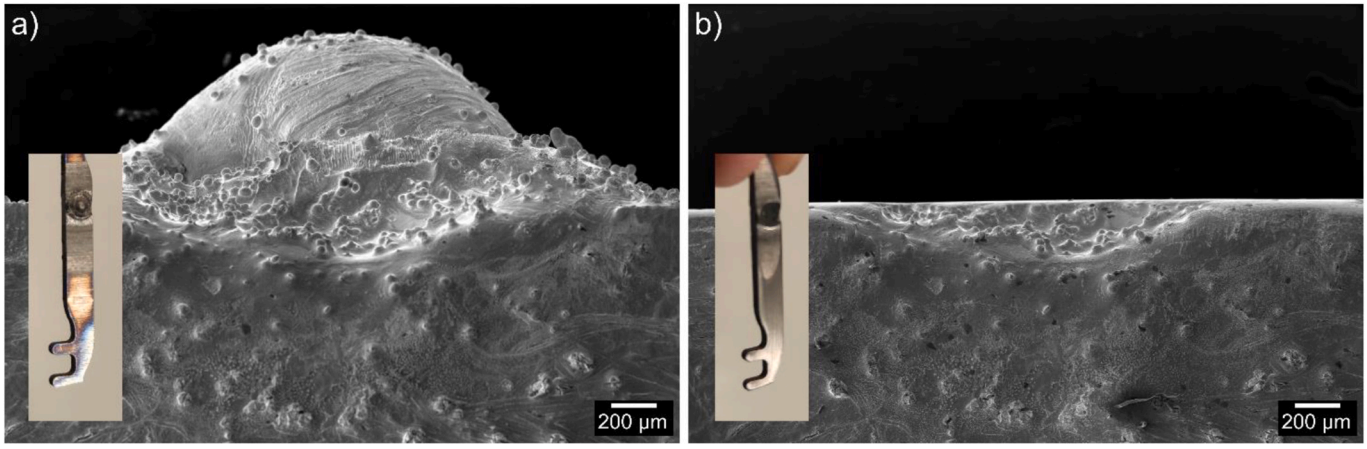

Fig. 15. Photographs and SEM images of a powder-based LMD specimen before (a) and after (b) the grinding post-processing operation.

to the interstitial oxygen detected by local EDS performed in areas devoid of oxide particles, which can provide strong solid-solution hardening in pure tantalum [20,28]. The finer grain size of the deposit made with the powder-based process is also responsible for the increase in hardness compared to the other specimen through the Hall-Petch mechanism. Zhou et al. [14] showed that an increase in the hardness of pure tantalum processed through LPBF is associated with improved wear resistance. Therefore, the high hardness attained after repair by both the wire- and powder-based process compared with the initial material may be beneficial to the durability of the electrodes used in the AMIT cyclotron.

3.4. Improvement of surface finish

Both the wire- and the powder-based processes created a prominent dome at the head of the repaired cathodes, as shown in the photographs of Fig. 4. In principle, a protruding surface could increase the local electric field at the electrode head compared to a flat surface [41], thus promoting the emission of electrons when the operating voltage is applied between the electrodes of the ion source. In addition, it could increase the service life of the electrodes by providing additional material against erosion crater formation. The main disadvantage of this design is the possible occurrence of short-circuits, which needs to be assessed by testing the restored cathodes in the AMIT cyclotron. The possibility of obtaining a flat surface with a finish comparable to that of the original parts was still demonstrated by removing the excess material from a test piece through a simple grinding operation (Fig. 15).

4. Conclusions

This work investigated the damage mechanisms to which the tantalum cathodes used in the ion source of the AMIT superconducting cyclotron are subjected during service and the possibility to restore them through wire- and powder-based laser metal deposition. The main outcomes can be summarised as follows:

(1) During operation, the impact of high-energy ions generates erosion craters at the cathode head and causes localised melting, abnormal grain growth, and hydrogen- and ion-irradiation-induced hardening.
(2) The wire-based repair involved the deposition of single dots of material inside the erosion craters. Laser preheating (1000 W for 1 s) eliminated the interface porosity and improved the adhesion with the substrate. Large columnar grains typical of additively manufactured tantalum did not develop because edge effects dominated solidification. EDS measurements displayed an oxygen content of ~0.8 wt%, similar to that of the original material (~0.5 wt%).
(3) Concentric rings were deposited in the powder-based process. Instabilities in the shielding gas flow resulted in ~3 wt% dissolved oxygen and finely dispersed oxide particles, leading to a microhardness of about 665.4 $HV_{0.5}$ due to solid-solution and precipitation strengthening, respectively.
(4) A simple post-processing operation effectively removed the excess material deposited during repair, resulting in a surface quality comparable to that of the original electrodes.

Supplementary data to this article can be found online at https://doi.org/10.1016/j.ijrmhm.2023.106364.

Declaration of Competing Interest

The authors declare that they have no known competing financial interests or personal relationships that could have appeared to influence the work reported in this paper.

Data availability

Data will be made available on request.

Acknowledgements

This work was carried out within the frame of the I.FAST project and has received funding from the European Union's Horizon 2020 Research and Innovation programme under grant agreement No 101004730. Open access funding was provided by Politecnico di Milano within the CRUI-CARE Agreement.

Authors would like to acknowledge the support given by Rasheed Michael Ishola and Ludovica Rovatti for SEM and EBSD analyses.

References

[1] R.W. Buckman, New applications for tantalum and tantalum alloys, JOM 52 (2000) 40–41, https://doi.org/10.1007/S11837-000-0100-6.
[2] S.M. Cardonne, P. Kumar, C.A. Michaluk, H.D. Schwartz, Tantalum and its alloys, Int. J. Refract. Met. Hard Mater. 13 (1995) 187–194, https://doi.org/10.1016/0263-4368(95)94023-R.
[3] L. Bartha, Positive-ion Sources, in: R. Hellborg (Ed.), Electrost. Accel. 473, 2005, pp. 192–221, https://doi.org/10.1007/3-540-27095-7_19.
[4] L. Garcia-Tabares, P. Abramian, J. Calero, J.L. Gutierrez, J. Munilla, D. Obradors, J. M. Perez, F. Toral, R. Iturbe, L. Minguez, J. Gomez, E. Rodilla, M. Bajko, M. Michels, D. Berkowitz, F. Haug, Development of a superconducting magnet for a compact cyclotron for radioisotope production, IEEE Trans. Appl. Supercond. 26 (2016) 13–16, https://doi.org/10.1109/TASC.2016.2548429.
[5] P. Calvo, D. Obradors, R. Varela, I. Podadera, C. Oliver, A. Estévez, M. Domínguez, C. Vázquez, F. Toral, L. García-Tabarés, J.M. Pérez, Experimental characterization

of the internal ion source for the AMIT compact cyclotron, Nucl. Instruments Methods Phys. Res. Sect. A Accel. Spectrometers, Detect. Assoc. Equip. 1025 (2022), https://doi.org/10.1016/j.nima.2021.166028.
[6] D. Obradors, M.B. Ahedo, P. Arce, J.M. Barcala, J. Calero, P. Calvo, M. A. Domínguez, A. Estévez, J.M. Figarola, A. Guirao, L. García-Tabarés, D. Gavela, P. Gómez, J.L. Gutierrez, J.I. Lagares, D. López, L.M. Martinez, J.I. Martinez, J. Munilla, C. Oliver, J.M. Perez, I. Podadera, E. Rodriguez, F. Toral, R. Varela, C. Vazquez, R. Iturbe, B. López, Characterization of the AMIT internal ion source with a devoted DC extraction test bench, in: IPAC 2017 - Proc. 8th Int. Part. Accel. Conf., 2017, pp. 1740–1742.
[7] G. Marinelli, F. Martina, S. Ganguly, S. Williams, Microstructure, hardness and mechanical properties of two different unalloyed tantalum wires deposited via wire + arc additive manufacture, Int. J. Refract. Met. Hard Mater. 83 (2019), https://doi.org/10.1016/j.ijrmhm.2019.104974.
[8] H.B. Michaelson, The work function of the elements and its periodicity, J. Appl. Phys. 48 (2008) 4729, https://doi.org/10.1063/1.323539.
[9] N.A. Mancheri, B. Sprecher, S. Deetman, S.B. Young, R. Bleischwitz, L. Dong, R. Kleijn, A. Tukker, Resilience in the tantalum supply chain, Resour. Conserv. Recycl. 129 (2018) 56–69, https://doi.org/10.1016/j.resconrec.2017.10.018.
[10] V.G. Smelov, A.V. Sotov, A.V. Agapovichev, Research on the possibility of restoring blades while repairing gas turbine engines parts by selective laser melting, IOP Conf. Ser. Mater. Sci. Eng. 140 (2016), 012019, https://doi.org/10.1088/1757-899X/140/1/012019.
[11] S. Yin, P. Cavaliere, B. Aldwell, R. Jenkins, H. Liao, W. Li, R. Lupoi, Cold spray additive manufacturing and repair: fundamentals and applications, Addit. Manuf. 21 (2018) 628–650, https://doi.org/10.1016/J.ADDMA.2018.04.017.
[12] R. Joey Griffiths, D.T. Petersen, D. Garcia, H.Z. Yu, Additive friction stir-enabled solid-state additive manufacturing for the repair of 7075 aluminum alloy, Appl. Sci. 9 (2019) 3486, https://doi.org/10.3390/APP9173486.
[13] A. Saboori, A. Aversa, G. Marchese, S. Biamino, M. Lombardi, P. Fino, Application of directed energy deposition-based additive manufacturing in repair, Appl. Sci. 9 (2019), https://doi.org/10.3390/app9163316.
[14] L. Zhou, T. Yuan, R. Li, J. Tang, G. Wang, K. Guo, Selective laser melting of pure tantalum: densification, microstructure and mechanical behaviors, Mater. Sci. Eng. A 707 (2017) 443–451, https://doi.org/10.1016/j.msea.2017.09.083.
[15] R. Wauthle, J. Van Der Stok, S.A. Yavari, J. Van Humbeeck, J.P. Kruth, A. A. Zadpoor, H. Weinans, M. Mulier, J. Schrooten, Additively manufactured porous tantalum implants, Acta Biomater. 14 (2015) 217–225, https://doi.org/10.1016/j.actbio.2014.12.003.
[16] J. Yang, X. Jin, H. Gao, D. Zhang, H. Chen, S. Zhang, X. Li, Additive manufacturing of trabecular tantalum scaffolds by laser powder bed fusion: mechanical property evaluation and porous structure characterization, Mater. Charact. 170 (2020), 110694, https://doi.org/10.1016/j.matchar.2020.110694.
[17] H.P. Tang, K. Yang, L. Jia, W.W. He, L. Yang, X.Z. Zhang, Tantalum bone implants printed by selective Electron beam manufacturing (SEBM) and their clinical applications, Jom. 72 (2020) 1016–1021, https://doi.org/10.1007/s11837-020-04016-8.
[18] A.A.A. Aliyu, K. Poungsiri, J. Shinjo, C. Panwisawas, R.C. Reed, C. Puncreobutr, K. Tumkanon, S. Kuimalee, B. Lohwongwatana, Additive manufacturing of tantalum scaffolds: processing, microstructure and process-induced defects, Int. J. Refract. Met. Hard Mater. 112 (2023), 106132, https://doi.org/10.1016/j.ijrmhm.2023.106132.
[19] G. Marinelli, F. Martina, S. Ganguly, S. Williams, Grain refinement in an unalloyed tantalum structure by combining wire+arc additive manufacturing and vertical cold rolling, Addit. Manuf. 32 (2020), 101009, https://doi.org/10.1016/j.addma.2019.101009.
[20] B. Guan, M. Xu, X. Yang, Y. Zhou, C. Li, Y. Ji, X. Liu, J. Li, D. Wang, J. Tang, G. Le, Microstructure and strengthening mechanisms of tantalum prepared using laser melting deposition, Int. J. Refract. Met. Hard Mater. 103 (2022), 105773, https://doi.org/10.1016/j.ijrmhm.2021.105773.
[21] V.K. Balla, S. Banerjee, S. Bose, A. Bandyopadhyay, Direct laser processing of a tantalum coating on titanium for bone replacement structures, Acta Biomater. 6 (2010) 2329–2334, https://doi.org/10.1016/j.actbio.2009.11.021.
[22] I. Shakhverdova, S. Nowotny, S. Thieme, F. Kubisch, E. Beyer, C. Leyens, Coaxial laser wire deposition, J. Phys. Conf. Ser. 1109 (2018), https://doi.org/10.1088/1742-6596/1109/1/012026.
[23] F. Brueckner, M. Riede, M. Müller, F. Marquardt, R. Willner, A. Seidel, E. Lopéz, C. Leyens, E. Beyer, Enhanced manufacturing possibilities using multi-materials: in laser metal deposition, LIA Today. 26 (2018) 10–12, https://doi.org/10.2351/1.5040639/1059497.
[24] F. Brueckner, M. Riede, F. Marquardt, R. Willner, A. Seidel, S. Thieme, C. Leyens, E. Beyer, Process characteristics in high-precision laser metal deposition using wire and powder, J. Laser Appl. 29 (2017), 022301, https://doi.org/10.2351/1.4983237.
[25] S. Semboshi, N. Masahashi, S. Hanada, Multiple cracking of tantalum by hydrogenation, Metall. Mater. Trans. A Phys. Metall. Mater. Sci. 34 A (2003) 685–690, https://doi.org/10.1007/s11661-003-0102-4.
[26] N.A. Pedrazas, T.E. Buchheit, E.A. Holm, E.M. Taleff, Dynamic abnormal grain growth in tantalum, Mater. Sci. Eng. A 610 (2014) 76–84, https://doi.org/10.1016/j.msea.2014.05.031.
[27] V. Livescu, J.F. Bingert, T.A. Mason, Deformation twinning in explosively-driven tantalum, Mater. Sci. Eng. A 556 (2012) 155–163, https://doi.org/10.1016/j.msea.2012.06.071.
[28] T. Schmitz, C. Hertl, E. Werner, U. Gbureck, J. Groll, C. Moseke, Oxygen diffusion hardening of tantalum coatings on cp-titanium for biomedical applications, Surf. Coat. Technol. 216 (2013) 46–51, https://doi.org/10.1016/j.surfcoat.2012.11.021.
[29] H. Matsui, H. Kimura, A. Kimura, The effect of hydrogen on the mechanical properties of high purity iron III. The dependence of softening in specimen size and charging current density, Mater. Sci. Eng. 40 (1979) 227–234, https://doi.org/10.1016/0025-5416(79)90193-9.
[30] Y. Zhao, M.Y. Seok, I.C. Choi, Y.H. Lee, S.J. Park, U. Ramamurty, J.Y. Suh, J. Il Jang, The role of hydrogen in hardening/softening steel: influence of the charging process, Scr. Mater. 107 (2015) 46–49, https://doi.org/10.1016/j.scriptamat.2015.05.017.
[31] Y. Murakami, T. Kanezaki, Y. Mine, Hydrogen effect against hydrogen embrittlement, Metall. Mater. Trans. A Phys. Metall. Mater. Sci. 41 (2010) 2548–2562, https://doi.org/10.1007/s11661-010-0275-6.
[32] I. Takagi, S. Nagaoka, K. Shirai, K. Moritani, H. Moriyama, Trapping of hydrogen in tantalum bombarded with helium-3 ions, Phys. Scr. T. 103 (2002) 121–124, https://doi.org/10.1238/physica.topical.103a00121.
[33] I. Ipatova, P.T. Wady, S.M. Shubeita, C. Barcellini, A. Impagnatiello, E. Jimenez-Melero, Characterisation of lattice damage formation in tantalum irradiated at variable temperatures, J. Microsc. 270 (2018) 110–117, https://doi.org/10.1111/JMI.12662.
[34] Q. Bao, Z. Li, B. Zhu, S. Liang, J. Zhu, M. Huang, L. Zhao, Y. Zhu, Influence of kinetic effect on interaction between edge dislocation and irradiated dislocation loops in BCC tantalum, Int. J. Plast. 165 (2023), 103603, https://doi.org/10.1016/j.ijplas.2023.103603.
[35] L. Thijs, M.L. Montero Sistiaga, R. Wauthle, Q. Xie, J.P. Kruth, J. Van Humbeeck, Strong morphological and crystallographic texture and resulting yield strength anisotropy in selective laser melted tantalum, Acta Mater. 61 (2013) 4657–4668, https://doi.org/10.1016/j.actamat.2013.04.036.
[36] R.A. Vandermeer, W.B. Snyder, Recovery and recrystallization in rolled tantalum single crystals, Metall. Trans. A. 10 (1979) 1031–1044, https://doi.org/10.1007/BF02811649.
[37] Y.H. Liu, S.F. Liu, J.L. Zhu, C. Deng, H.Y. Fan, L.F. Cao, Q. Liu, Strain path dependence of microstructure and annealing behavior in high purity tantalum, Mater. Sci. Eng. A 707 (2017) 518–530, https://doi.org/10.1016/j.msea.2017.09.097.
[38] T. DebRoy, H.L. Wei, J.S. Zuback, T. Mukherjee, J.W. Elmer, J.O. Milewski, A. M. Beese, A. Wilson-Heid, A. De, W. Zhang, Additive manufacturing of metallic components – process, structure and properties, Prog. Mater. Sci. 92 (2018) 112–224, https://doi.org/10.1016/j.pmatsci.2017.10.001.
[39] I. Dey, M. Fabbri, S. Gemmet, M. Dalaee, M. Wessel, K. Wegener, Manufacturing a prototype with laser direct metal deposition and laser welding made from martensitic steel 1.4313, Int. J. Adv. Manuf. Technol. 124 (2023) 1993–2009, https://doi.org/10.1007/s00170-022-10606-4.
[40] S.V.J. Chandra, S. Uthanna, G.M. Rao, Effect of substrate temperature on the structural, optical and electrical properties of dc magnetron sputtered tantalum oxide films, Appl. Surf. Sci. 254 (2008) 1953–1960, https://doi.org/10.1016/j.apsusc.2007.08.005.
[41] N. Shipman, Experimental Study of DC Vacuum Breakdown and Application to High-gradient Accelerating Structures for CLIC (Ph.D. thesis), 2015.